A community benchmark for viscoplastic thermal convection in a 2-D square box

N. Tosi[1,2], C. Stein[3], L. Noack[4], C. Hüttig[2], P. Maierová[5], H. Samuel[6,7], D. R. Davies[8], C. R. Wilson[9], S. C. Kramer[10], C. Thieulot[11,12], A. Glerum[11,13], M. Fraters[11], W. Spakman[11,12], A. Rozel[14], and P. J. Tackley[14]

[1]Department of Astronomy and Astrophysics, Technische Universität Berlin, Berlin, Germany, [2]Department of Planetary Physics, German Aerospace Center, Berlin, Germany, [3]Institute for Geophysics, Westfälische Wilhelms-Universität Münster, Münster, Germany, [4]Department of Reference Systems and Geodynamics, Royal Observatory of Belgium, Brussels, Belgium, [5]Center for Lithospheric Research, Czech Geological Survey, Prague, Czech Republic, [6]Université de Toulouse, UPS-OMP, IRAP, Toulouse, France, [7]CNRS, IRAP, Toulouse, France, [8]Research School of Earth Sciences, Australian National University, Canberra, Australian Capital Territory, Australia, [9]Lamont-Doherty Earth Observatory, Columbia University, Palisades, New York, USA, [10]Department of Earth Science and Engineering, Imperial College, London, UK, [11]Department of Earth Sciences, Utrecht University, Utrecht, Netherlands, [12]Centre of Earth Evolution and Dynamics, University of Oslo, Oslo, Norway, [13]Netherlands Research Centre for Integrated Solid Earth Science, Amsterdam, Netherlands, [14]Department of Geophysical Fluid Dynamics, ETH Zurich, Zurich, Switzerland

Abstract Numerical simulations of thermal convection in the Earth's mantle often employ a pseudoplastic rheology in order to mimic the plate-like behavior of the lithosphere. Yet the benchmark tests available in the literature are largely based on simple linear rheologies in which the viscosity is either assumed to be constant or weakly dependent on temperature. Here we present a suite of simple tests based on nonlinear rheologies featuring temperature, pressure, and strain rate-dependent viscosity. Eleven different codes based on the finite volume, finite element, or spectral methods have been used to run five benchmark cases leading to stagnant lid, mobile lid, and periodic convection in a 2-D square box. For two of these cases, we also show resolution tests from all contributing codes. In addition, we present a bifurcation analysis, describing the transition from a mobile lid regime to a periodic regime, and from a periodic regime to a stagnant lid regime, as a function of the yield stress. At a resolution of around 100 cells or elements in both vertical and horizontal directions, all codes reproduce the required diagnostic quantities with a discrepancy of at most ~3% in the presence of both linear and nonlinear rheologies. Furthermore, they consistently predict the critical value of the yield stress at which the transition between different regimes occurs. As the most recent mantle convection codes can handle a number of different geometries within a single solution framework, this benchmark will also prove useful when validating viscoplastic thermal convection simulations in such geometries.

1. Introduction

Benchmark tests are an invaluable tool for verifying the correctness of algorithm implementations and the accuracy of numerical solutions. However, modern simulations of mantle convection often include several complexities for which such tests either do not exist or, when available, only permit the validation of features that need to be considered separately from one another. In recent years, a number of benchmark studies based on code intercomparison have been proposed to verify various important aspects of the dynamics of the Earth's and planetary interiors such as incompressible thermal convection in 2-D [*Blankenbach et al.*, 1989; *Travis et al.*, 1990] and 3-D Cartesian geometry [*Busse et al.*, 1994], in spherical shell geometry [*Zhong et al.*, 2008], in the presence of compositional variations [*van Keken et al.*, 1997] or accounting for compressibility and non-Boussinesq effects [*King et al.*, 2010], kinematic-dynamic modeling of the thermal structure of subduction zones [*van Keken et al.*, 2008], subduction dynamics with a free surface [*Schmeling et al.*, 2008], and the techniques with which the latter can be modeled [*Crameri et al.*, 2012], or brittle deformation of the crust and lithosphere [*Buiter et al.*, 2006]. Simulations of global-scale convection in the Earth's mantle routinely employ a pseudoplastic rheology to account for the mobility of the upper thermal boundary layer (e.g., *Trompert and Hansen* [1998], *Tackley* [2000], *Stein et al.* [2004], *van Heck and Tackley* [2008],

and *Foley and Becker*, 2009, to mention only a few studies based on three-dimensional simulations). Nevertheless, to date, no benchmark test is available to verify numerical implementations of Rayleigh-Bénard convection of a so-called Bingham fluid (i.e., a fluid with yield stress) with negligible inertia in which the viscosity also depends strongly on temperature, thereby naturally leading to plastic yielding at low temperature and high stresses, and to strengthless deformation at high temperatures as appropriate for modeling (Newtonian) mantle creep.

We adopt an approach similar to that of the classic benchmark suite introduced by *Blankenbach et al.* [1989] to validate thermal convection simulations with constant and weakly temperature-dependent viscosity in a 2-D Cartesian box. Because of its simplicity and despite its agedness, this benchmark has become de facto a standard for the geodynamics community. The "Blankenbach benchmark" is not only continuously used to validate modern convection codes [e.g., *Gerya and Yuen*, 2003; *Davies et al.*, 2011; *Leng and Zhong*, 2011; *Kronbichler et al.*, 2012] but also represents a practical starting point upon which more complex benchmark scenarios can be built, as demonstrated by the series of tests for compressible anelastic convection proposed by *King et al.* [2010]. Here we extend this classic benchmark suite by considering a rheological formulation with a viscosity that, besides being temperature and pressure dependent, also depends nonlinearly on the strain rate. In particular, we focus on the role of the yield stress, showing how this parameter, by controlling the viscosity distribution at low temperatures and high stresses, is ultimately responsible for the mode of surface deformation: from mobile lid (corresponding to low values of the yield stress), to episodic mobilization (for intermediate values), to stagnant lid (for large values).

In the following section, we introduce the set of nondimensional equations that we solved along with the rheological relations used to define the viscosity field. In section 3, we describe the benchmark tests, and in section 4, we summarize the main features of the participating codes. Section 5 contains the benchmark results, and section 6 completes the paper with a brief summary.

2. Conservation Equations and Rheology

We solve the nondimensional equations for Boussinesq convection in a fluid with negligible inertia (i.e., with infinite Prandtl number) heated from below and cooled from above in a 2-D square cavity with free-slip boundaries, insulating sidewalls and isothermal top and bottom boundaries (see section 3 for a precise description of the boundary conditions). A coordinate system xy is chosen with the origin of the vertical y axis located at the bottom of the domain. As usual in mantle convection simulations, the length is scaled with the mantle thickness D, the time t with the diffusion time scale D^2/κ (where κ is the thermal diffusivity), the velocity $\boldsymbol{u}$ with κ/D, the temperature T with the temperature drop across the mantle ΔT, the viscosity η with a reference value η_0, and, in turn, the stress τ with $\eta_0\kappa/D^2$. Assuming constant thermal diffusivity and thermal expansivity (α) and variable viscosity, the conservation equations of mass, linear momentum, and thermal energy read, respectively,

$$\nabla \cdot \boldsymbol{u} = 0, \tag{1}$$

$$-\nabla p + \nabla \cdot \tau = Ra\, T \boldsymbol{e}_y, \tag{2}$$

$$\frac{\partial T}{\partial t} + \boldsymbol{u} \cdot \nabla T = \nabla^2 T, \tag{3}$$

where p is the dynamic pressure, τ is the deviatoric stress tensor given by

$$\tau = 2\eta\dot{\epsilon} = \eta(\nabla \boldsymbol{u} + (\nabla \boldsymbol{u})^t), \tag{4}$$

where $\dot{\epsilon}$ is the strain rate tensor, $()^t$ denotes the operation of transposition, $\boldsymbol{e}_y$ is the unit vector pointing upward in the vertical direction, and Ra is the Rayleigh number:

$$Ra = \frac{\rho g \alpha \Delta T D^3}{\kappa \eta_0}, \tag{5}$$

where ρ, g, α, and η_0 are reference density, gravity acceleration, thermal expansivity, and reference viscosity, respectively, all of which are assumed to be constant. The viscosity field η is calculated as the harmonic

average between a linear part η_{lin} that depends on temperature only or on temperature and depth z (with $z = 1-y$), and a nonlinear, plastic part η_{plast} dependent on the strain rate

$$\eta(T, z, \dot{\epsilon}) = 2 \left(\frac{1}{\eta_{lin}(T, z)} + \frac{1}{\eta_{plast}(\dot{\epsilon})} \right)^{-1}.$$ (6)

The linear part is given by the linearized Arrhenius law (the so-called Frank-Kamenetskii approximation [*Frank-Kamenetskii*, 1969])

$$\eta_{lin}(T, z) = \exp(-\gamma_T T + \gamma_z z),$$ (7)

where $\gamma_T = \ln(\Delta\eta_T)$ and $\gamma_z = \ln(\Delta\eta_z)$ are parameters controlling the total viscosity contrast due to temperature ($\Delta\eta_T$) and pressure ($\Delta\eta_z$). The nonlinear part is given by [e.g., *Trompert and Hansen*, 1998]

$$\eta_{plast}(\dot{\epsilon}) = \eta^* + \frac{\sigma_Y}{\sqrt{\dot{\epsilon} : \dot{\epsilon}}},$$ (8)

where η^* is a constant representing the effective viscosity at high stresses [*Stein et al.*, 2014] and σ_Y is the yield stress, also assumed to be constant. In 2-D, the denominator in the second term of equation (8) is given explicitly by

$$\sqrt{\dot{\epsilon} : \dot{\epsilon}} = \sqrt{\dot{\epsilon}_{ij}\dot{\epsilon}_{ij}},$$ (9)

$$= \sqrt{\left(\frac{\partial u_x}{\partial x}\right)^2 + \frac{1}{2}\left(\frac{\partial u_x}{\partial y} + \frac{\partial u_y}{\partial x}\right)^2 + \left(\frac{\partial u_y}{\partial y}\right)^2}.$$ (10)

The viscoplastic flow law (equation (6)) leads to linear viscous deformation at low stresses (equation (7)) and to plastic deformation for stresses that exceed σ_Y (equation (8)), with the decrease in viscosity limited by the choice of η^* (see *Stein et al.* [2014] for a discussion of the combined role of η^* and σ_Y on the resulting convective regime).

3. Benchmark Description

In all cases that we present, the domain is a two-dimensional square box. The mechanical boundary conditions are for all boundaries free slip with no flux across, i.e., $\tau_{xy} = \tau_{yx} = 0$ and $\boldsymbol{u} \cdot \boldsymbol{n} = 0$, where $\boldsymbol{n}$ denotes the outward normal to the boundary. Concerning the energy equation, the bottom and top boundaries are isothermal, with the temperature T set to 1 and 0, respectively, while sidewalls are assumed to be insulating, i.e., $\partial T/\partial x = 0$. The initial distribution of the temperature field is prescribed as follows:

$$T(x, y) = (1-y) + A\cos(\pi x)\sin(\pi y),$$ (11)

where $A = 0.01$ is the amplitude of the initial perturbation.

In Table 1, we list the benchmark cases according to the parameters used. In all tests, the reference Rayleigh number is set at the surface ($y = 1$) to 10^2, and the viscosity contrast due to temperature $\Delta\eta_T$ is 10^5, implying therefore a maximum effective Rayleigh number of 10^7 for $T = 1$. Cases 3, 4, 5a, and 5b employ in addition a depth-dependent rheology with viscosity contrast $\Delta\eta_z = 10$. Cases 1 and 3 assume a linear viscous rheology that leads to a stagnant lid regime. Cases 2 and 4 assume a viscoplastic rheology that leads instead to a mobile lid regime. Case 5a also assumes a viscoplastic rheology but a higher yield stress, which ultimately causes the emergence of a strictly periodic regime. The setup of Case 5b is identical to that of Case 5a but the test consists in running several simulations using different yield stresses. Specifically, we varied σ_Y between 3 and 5 in increments of 0.1 in order to identify the values of the yield stress corresponding to the transition from mobile to periodic and from periodic to stagnant lid regime.

For Cases 1–4, all participants were requested to report a number of diagnostic quantities to be measured after reaching steady state. Specifically, average temperature

$$\langle T \rangle = \int_0^1 \int_0^1 T\, dxdy, \tag{12}$$

top and bottom Nusselt numbers

$$Nu_{\text{top/bot}} = -\int_0^1 \frac{\partial T}{\partial y}\bigg|_{y=1/y=0} dx, \tag{13}$$

root-mean-square (RMS) velocity over the whole domain, over the surface, as well as the maximum horizontal velocity at the surface

$$u_{\text{RMS}} = \left(\int_0^1 \int_0^1 \left(u_x^2 + u_y^2 \right) dxdy \right)^{1/2}, \tag{14}$$

$$u_{\text{RMS}}^{\text{surf}} = \left(\int_0^1 u_x^2 \bigg|_{y=1} dx \right)^{1/2}, \tag{15}$$

$$u_{\text{max}}^{\text{surf}} = \max(u_x)|_{y=1}, \tag{16}$$

maximum and minimum viscosity over the whole domain (for Cases 2, 3, and 4)

$$\eta_{\text{max}} = \max_{(x,y)\in[0,1]} (\eta(x,y)), \tag{17}$$

$$\eta_{\text{min}} = \min_{(x,y)\in[0,1]} (\eta(x,y)), \tag{18}$$

average rate of work done against gravity

$$\langle W \rangle = \int_0^1 \int_0^1 T u_y\, dxdy, \tag{19}$$

and average rate of viscous dissipation

$$\langle \Phi \rangle = \int_0^1 \int_0^1 \tau_{ij} \dot{\epsilon}_{ij}\, dxdy. \tag{20}$$

In steady state, if thermal energy is accurately conserved, the difference between $\langle W \rangle$ and $\langle \Phi \rangle / Ra$ must vanish [e.g., *King et al.*, 2010], so we also compute the percentage error

$$\delta = \frac{\left| \langle W \rangle - \dfrac{\langle \Phi \rangle}{Ra} \right|}{\max\left(\langle W \rangle, \dfrac{\langle \Phi \rangle}{Ra} \right)} \times 100\%. \tag{21}$$

In addition, all participants carried out resolution tests for Cases 1 and 2 (section 5.2). For these two cases, we also reported extrapolated steady state solutions based on the Richardson technique [e.g., *Roache*, 1997].

For Case 5a, after reaching a strictly periodic regime, we calculated the period P of the cycle as well as the maximum and minimum values of $\langle T \rangle$, Nu_{top}, u_{RMS}, and $\langle \Phi \rangle$ (section 5.3). Finally, for Case 5b, in those cases where a steady state was reached (either in mobile or stagnant lid regime), we only reported the surface Nusselt number Nu_{top}, while, in case of periodic solution, we reported the maximum and minimum value of Nu_{top} averaged over 10 cycles (section 5.4).

4. Description of the Participating Codes

In the following subsections, we provide a brief description of the various codes. We first describe codes based on the finite volume method (YACC, Plaatjes, CHIC, GAIA, StreamV, and StagYY), then those based on the finite element method (FEniCS, Fluidity, ELEFANT, and ASPECT), and finally the only spectral code involved (MC3D). Furthermore, in Table S1 of supporting information, we listed a number of geodynamic benchmark studies indicating whether each code has been validated or not against them.

Table 1. Benchmark Cases and Corresponding Parameters[a]

Case	Ra	$\Delta\eta_T$	$\Delta\eta_y$	η^*	σ_Y	Convective Regime
1	10^2	10^5	1			Stagnant lid
2	10^2	10^5	1	10^{-3}	1	Mobile lid
3	10^2	10^5	10			Stagnant lid
4	10^2	10^5	10	10^{-3}	1	Mobile lid
5a	10^2	10^5	10	10^{-3}	4	Periodic
5b	10^2	10^5	10	10^{-3}	3–5	Mobile lid-periodic-stagnant lid

[a]In Cases 1 and 3, the viscosity is directly calculated from equation (7), while for Cases 2, 4, 5a, and 5b, we used equation (6). For a given mesh resolution, Case 5b requires running simulations with yield stress varying between 3 and 5 (see text for details).

4.1. YACC

YACC (Yet Another Convection Code), developed by N. Tosi, is a Fortran 90 code based on a staggered-grid, control-volume discretization of the conservation equations [*Tosi et al.*, 2010; *King et al.*, 2010]. For each cell of the domain, the Stokes equation (2) is solved for horizontal and vertical velocity at staggered nodes together with the continuity equation (1), which is explicitly integrated for the pressure located at cell centers [e.g., *Gerya and Yuen*, 2003]. The nonlinearity due to the strain rate dependence of the viscosity is treated via underrelaxed Picard iterations. The thermal energy equation (3) is solved by means of a semi-Lagrangian operator splitting method [*Spiegelman and Katz*, 2006]. The temperature field, defined at non-staggered nodes (i.e., cell corners), is first advected through a semi-Lagrangian scheme with bicubic interpolation. A Crank-Nicolson scheme is then employed to integrate the diffusion equation with the advected temperature acting as a source term. Both linear systems arising from the discretization of equations (1)–(3) are solved using the parallel direct sparse solver MUMPS [*Amestoy et al.*, 2001, 2006]. For the main Cases 1–5a, we used a uniform resolution of 100 cells in both vertical and horizontal directions, with all diagnostic quantities computed using nonstaggered nodal solutions of temperature and velocity (note that the latter require a linear interpolation from the staggered nodes).

YACC is freely available. The Fortran source code as well as a set of C-shell scripts for output visualization based on the Generic Mapping Tool [*Wessel et al.*, 2013] can be downloaded from the repository https://bitbucket.org/7nic9/yacc-yet-another-convection-code. Input files to reproduce the benchmark tests of this study are available upon request from N. Tosi.

4.2. Plaatjes

Plaatjes (C. Stein) employs a staggered grid, finite volume method for spatial discretization and the implicit Θ-method (with Θ=0.5, corresponding to the Crank-Nicolson method) for temporal discretization with spatial discretization and time stepping done by using second-order methods [*Trompert and Hansen*, 1996]. The discrete system of equations is solved iteratively applying the linear multigrid method with SIMPLER as smoother [e.g., *Patankar*, 1980] where first the energy equation is solved with Jacobi iterations, then the pressure correction is iterated by further multigrid iterations with Jacobi as smoother, and finally the velocity is updated using Gauss-Seidel iterations. For the multigrid method, a cell-centered coarsening is applied so that in 2-D a coarse grid cell is obtained by combining four fine grid cells. The successive halving of the number of grid points thus requires the following condition for the number of finest grid points: $N_x = 2^{L_x}$ and $N_y = 2^{L_y}$ with L_x and $L_y \in \mathbb{N}$. The resolution used for the benchmark problems 1–5a is $N_x = N_y = 128$ with a uniform grid spacing in the horizontal direction and nonuniform grid spacing in the vertical direction (i.e., a refinement near the top and bottom boundaries as in *Trompert and Hansen* [1996]).

4.3. CHIC

CHIC (Coupling Habitability, Interior and Crust) is a Fortran 90 code developed at the Royal Observatory of Belgium by L. Noack and colleagues [*Noack et al.*, 2015]. It treats 2-D and 3-D Cartesian boxes as well as 2-D spherical geometries (spherical annulus and cylindrical geometry) in Cartesian or polar coordinates, respectively. The finite volume method is used to solve the partial differential equations on staggered grids. For this benchmark, the continuity and momentum equations are solved implicitly in one linear system where a viscosity-dependent penalty term is applied in the continuity equation. The thermal energy equation is solved implicitly with second-order accuracy. Both linear systems (continuity-momentum and energy) are solved iteratively in each time step until the temperature converges. Here the PARDISO solver is applied

[*Schenk and Gärtner*, 2000, 2006] for solving the linear systems of equations. For Cases 1–5a, a uniform grid with 80 cells in both vertical and horizontal directions is employed.

4.4. GAIA

The Generic Automaton for planetary Interior Analysis GAIA is a Stokes-flow and energy solver intended for mantle convection applications written in C++ by C. Hüttig. The code allows high-performance computing with a domain-decomposition technique [*Hüttig and Stemmer*, 2008a] that enables GAIA, in combination with MPI, to efficiently run on thousands of compute cores. It is based on a finite volume discretization of the conservation equations (1–3) expressed in Cartesian coordinates. It can handle different geometries, from 2-D and 3-D rectangular boxes to 2-D cylindrical and 3-D spherical shells or full spheres. The computational domain can be meshed with structured or fully unstructured grids representing Voronoi diagrams obtained from a Delaunay triangulation of given sets of generator points [*Hüttig and Stemmer*, 2008b]. GAIA uses a colocated arrangement in which all field variables are defined at the center of each control volume. In its latest implementation [*Hüttig et al.*, 2013], GAIA solves the momentum and continuity equations for the primitive variables u and p by explicitly integrating equation (1) for the pressure [e.g., *Gerya and Yuen*, 2003]. The energy equation (3) is solved with a fully implicit, three-level scheme with second-order accuracy in space and time [*Harder and Hansen*, 2005]. The advection term follows a second-order MUSCL (Monotonic Upstream-Centered Scheme for Conservation Laws) [*van Leer*, 1979] scheme combined with a superbee-limiter to prevent unphysical oscillations near sharp gradients that can accompany the MUSCL advection [e.g., *Roe*, 1986]. In addition, the nonlinear coupling between momentum and energy equations is treated via Picard iterations. The two linear systems arising from the discretization of the conservation equations are solved with the BiCGStab(ℓ) Krylov subspace method [*Sleijpen and Fokkema*, 1993] in combination with a simple Jacobi preconditioner. The grid employed in the benchmarks 1–5a consists of 100 cells in both directions with refinement near the four domain boundaries.

4.5. StreamV

StreamV is a finite volume thermochemical convection code written in Fortran 90 by H. Samuel [*Samuel and Evonuk*, 2010; *Samuel*, 2012, 2014]. The code solves for the conservation of momentum subject to the incompressibility constraint and the conservation of energy and/or composition in various 2-D geometries (Cartesian, cylindric, 3-D axi-symmetric) and in 3-D Cartesian domains. The code has been successfully benchmarked against analytical and numerical solutions of the governing equations [*Blankenbach et al.*, 1989; *van Keken et al.*, 1997] including variable (linear) viscous rheology. For 2-D geometries, a pure stream function formulation is used to solve the Navier Stokes equation, resulting in a biharmonic equation for the stream function. The latter is defined at nodal points, leading to a natural control volume formulation on a staggered grid, with velocity components located at the center of each control volume face, and satisfying automatically mass conservation. While coupled geometric multigrid and preconditioned biconjugate gradient solvers are available for solving equations (1) and (2), the tests performed in this study used the MUMPS [*Amestoy et al.*, 2001, 2006] direct solver library. An underrelaxation procedure is used to calculate the solution for nonlinear viscosity cases. In the present study, the conservation of energy is solved with a purely Eulerian approach, using advection-diffusion operator splitting. The diffusion terms are discretized using a standard second-order scheme. The advective terms are discretized using either a conservative upwind-biased Weighted Essentially Non-Oscillatory (WENO) scheme [*Jiang and Shu*, 1996], or a monotone second-order Total Variation Diminishing (TVD) scheme with various flux limiters [*Roe*, 1986]. The time integration is performed via an explicit TVD Runge-Kutta (RK) scheme of either first, second, or third order [*Harten*, 1983] with CFL time stepping. For most cases presented here, second-order schemes with the van Leer flux limiter and fifth-order WENO schemes were used, along with first-order RK time integration. As for temperature, viscosity is defined at cell centers and harmonic averaging is used to calculate viscosity values at other grid locations. Calculations were performed on domains discretized using square control volumes. Viscous dissipation, RMS velocities were calculated using cell-centered values. A uniform grid with 80 $\times$ 80 cells was used in Cases 1–5a.

4.6. StagYY

StagYY is a finite-volume/finite difference Fortran 90/MPI convection code developed by P. Tackley and coworkers [*Tackley*, 1993; *Tackley and Xie*, 2003; *Hernlund and Tackley*, 2008; *Tackley*, 2008]. The Stokes, continuity, and advection-diffusion equations are solved on a staggered grid in Cartesian or spherical geometry,

in two or three dimensions. The velocity components are defined at the cell boundaries perpendicular to their direction and pressure is defined at cell centers. In this study, a SIMPLER-like method [*Patankar*, 1980] is used to iterate on velocity and pressure fields, and is incorporated into multigrid F-cycles to increase convergence rate. The MPDATA scheme [*Smolarkiewicz*, 1984] has been used for the advection of temperature, and diffusion is solved through an explicit scheme, with a Courant number fixed to 0.8. Plasticity is converged through standard underrelaxed Picard iterations. The viscosity η_n at Picard step n is found using the viscosity of the previous Picard step η_{n-1} and the viscosity $\eta_n(T, y, \dot{\epsilon})$ (cf. equation (6))

$$\eta_n = \eta_{n-1}^{1/2} \eta_n(T, y, \dot{\epsilon})^{1/2}. \tag{22}$$

At each new viscosity field, the Stokes and continuity equations are solved again until the average of the velocity-pressure residuals is smaller than 10^{-3}. In Cases 1–5a, we used a mesh consisting of 128×128 grid points with vertical refinement in the top and bottom boundary layers.

4.7. FEniCS

FEniCS (P. Maierová) is a freely downloadable software package for automated solution of partial differential equations using finite element methods [*Logg et al.*, 2012]. Its main component DOLFIN is a C++ library with a Python interface that provides tools for definition, discretization, and solution of the equations. An important feature is the Unified Form Language (UFL), which is used for the definition of finite element spaces and expression of equations in a nearly symbolic notation. Different solvers and preconditioners can be applied to the linear equation systems. Provided that appropriate solvers and mesh partitioners are chosen, DOLFIN can run in parallel (with MPI or OpenMP). The applicability of FEniCS to the modeling of thermochemical mantle convection was demonstrated by *Vynnytska et al.* [2013]. The presented implementation of the test cases uses triangular P2–P1 velocity-pressure elements and quadratic elements for temperature. The nonlinearity in the momentum conservation equations is treated via Newton method implemented in DOLFIN. Both linear systems are solved using the direct solver MUMPS [*Amestoy et al.*, 2001, 2006]. A first-order implicit scheme is used for time stepping. The mesh resolution adopted for Cases 1–5a was of 80 triangular elements in both vertical and horizontal directions. FEniCS is freely available and can be downloaded at the address: http://http://fenicsproject.org. Input files to reproduce the benchmark tests of this study are available upon request from P. Maierová.

4.8. Fluidity

Fluidity is a general purpose computational fluid dynamics code, which was recently extended to solve the Stokes and accompanying field equations that are relevant to geodynamics by *Davies et al.* [2011] and *Kramer et al.* [2012]. The code uses unstructured simplex meshes, which enable the straightforward representation of complex geometries. Fluidity supports both continuous and discontinuous Galerkin finite element discretizations, in addition to control-volume discretizations. However, for the purposes of this benchmark, the governing equations are discretized using a continuous Galerkin finite element approach. In all Fluidity results that follow, a P2–P1 velocity-pressure element pair is used for the Stokes system, which consists of piecewise quadratic basis functions (P2) for velocity and piecewise linear basis functions (P1) for pressure. The mass and momentum conservation equations are solved using a Schur Complement Reduction approach: for velocity solves, the Conjugate Gradient (CG) method with an algebraic multigrid preconditioner is used (GAMG from the PETSc library [*Balay et al.*, 1997]), with the pressure correction equation solved through the FGMRES Krylov method, preconditioned with a pressure mass matrix, scaled by the local inverse of viscosity (for further details, see *May and Moresi* [2008] and *Davies et al.* [2011]). For solution of the discretized energy equation, piecewise linear, continuous elements are used. As with the benchmark results presented in *Davies et al.* [2011] and *Le Voci et al.* [2014], the results presented herein were found to be sufficiently smooth that no stabilization of the Galerkin discretization (e.g., SUPG [*Hughes and Brooks*, 1982]) was required. The GMRES Krylov subspace method is used to solve for temperature with successive over relaxation (SOR) preconditioning and a Crank-Nicholson scheme is used for time stepping. Nonlinear coupling between temperature and velocity is handled via a Picard iteration. The mesh resolution adopted for Cases 1–5a was of 128 triangular elements in both vertical and horizontal directions.

4.9. ELEFANT

ELEFANT borrows largely from the FANTOM code [*Thieulot*, 2011], but it also brings a number of critical improvements compared to its predecessor [*Thieulot*, 2014]. It is a finite element code, based on bilinear

velocity-constant pressure (Q1-P0) elements and a penalty formulation. Markers are used to track material properties and are advected by means of a fourth-order Runge-Kutta scheme in space. The direct solver MUMPS [*Amestoy et al.*, 2001, 2006] is used to solve the large linear systems arising from the discretized equations. The Streamline Upwind Petrov-Galerkin method is used to stabilize the advection term of the energy equation. ELEFANT has been extensively benchmarked. A mesh consisting of 100 × 100 quadrilateral elements was used for the benchmark Cases 1–5a.

4.10. ASPECT

ASPECT (short for Advanced Solver for Problems in Earths ConvecTion) is a new open source finite element code [*Kronbichler et al.*, 2012]. The code is directly built upon deal.ii [*Bangerth et al.*, 2007], which is a general-purpose finite element library, TRILINOS [*Heroux et al.*, 2005], which provides scalable and parallel solvers, and p4est [*Burstedde et al.*, 2011], which builds distributed adaptive meshes in parallel. ASPECT relies on the use of modern numerical methods such as adaptive mesh refinement, linear and nonlinear solvers, and stabilization of transport-dominated processes. These modern methods, together with high-order elements, ensure highly accurate solutions and good scaling up to several thousand processors. For the benchmark problems presented in this paper, Q2Q1 elements are used on uniform grids. At every time step, the energy and Stokes equations are solved and updated in turn until the solution has converged. These so-called nonlinear iterations account for the temperature, strain rate, and composition-dependent viscosity. For the benchmark tests 1–5a, we used 64 elements in both horizontal and vertical directions.

ASPECT is freely available and can be downloaded at the address: http://aspect.dealii.org. Input files to reproduce the benchmark tests of this study are available upon request from A. Glerum.

4.11. MC3D

The hybrid spectral and finite-difference code, MC3D (C. Stein), is second-order accurate in time and space where the explicit finite difference scheme is used to solve the heat transport equation and the spectral formulation is employed to solve for the velocities [*Gable et al.*, 1991]. In the spectral formulation, the horizontal Fourier transforms rather than local functions are used, which makes variable viscosity more difficult to handle. As *Stein and Hansen* [2014] have shown that layered temperature-dependent viscosity is a suitable approximation for the full temperature dependence, MC3D only uses the horizontally averaged strain rate and temperature (geotherm) to compute the viscosity [*Stein et al.*, 2014]. Here the arithmetic mean is used as averaging scheme. Note that *Stein and Hansen* [2014] investigated different averaging schemes for thermoviscous convection. As the differences in the results were only minor, we do not expect the averaging scheme used to model the strain rate dependence of the viscosity to exert a significant impact on the results. Numerical grid resolution for the benchmark problems 1–5a is chosen to be 100 × 100 with a uniform grid spacing in horizontal and vertical directions.

5. Benchmark Results

5.1. Cases 1–4: Steady State Solutions

In Table 2, we list the results of the five benchmark Cases 1–5a from all participating codes. For Cases 1–4, Figures 1–4 show the distribution of the nondimensional temperature, viscosity, RMS velocity, and square root of the second invariant of the stress tensor (i.e., $\tau_{II} \equiv \sqrt{\tau : \tau/2}$), as well as the corresponding laterally averaged profiles. All codes produce a one-cell, steady state solution obtained by explicit time integration of the conservation equations, namely Picard iterations are only employed to ensure convergence of the nonlinear viscosity within single time steps but not enforce steady state by avoid calculating explicitly the time derivative in the temperature in equation (3).

As anticipated in section 2, because of the temperature dependence of the viscosity, in Cases 1 and 3 (Figures 1 and 3), a lid of variable thickness develops that insulates the underlying fluid maintaining its temperature uniformly high ($T \sim 0.9$). In Cases 2 and 4 (Figures 2 and 4), where the strain rate dependence of the viscosity is also taken into account, the surface becomes mobile; the uppermost cold layers participate in the convection and cool the interior causing its temperature to reduce to $\sim$0.5 (i.e., the value that characterizes isoviscous convection in a Cartesian box). Around the two upper corners of the domain, where the

Table 2. Benchmark Results From All Participating Codes for Cases 1–5a[a]

Code Resolution	YACC 100 × 100	Plaatjes 128×128r	CHIC 80 × 80	GAIA 100r×100r	StreamV 80 × 80	StagYY 128×128r	FEniCS 80 × 80	Fluidity 128 × 128	ELEFANT 100 × 100	ASPECT 64 × 64	MC3D 100 × 100
Case 1											
$\langle T \rangle$	0.7767	0.7759	0.7758	0.7759	0.776	0.776	0.7759	0.7758	0.7758	0.7768	0.779
Nu_{top}	3.4298	3.4159	3.4260	3.4213	3.4091	3.419	3.5889	3.4253	3.4214	3.4305	3.3129
Nu_{bot}	3.3143	3.4159	3.4259	3.4213	3.4091	3.419	3.4231	3.3795	3.313	3.4142	3.3139
u_{RMS}	251.7997	249.54	249.2985	250.0738	252.0906	249.541	249.5730	248.9252	249.134	251.3069	296.6156
u_{RMS}^{surf}	1.8298	1.878	1.8999	1.8836	1.8823	1.8723	1.8698	1.8474	1.8642	1.8695	1.1114
u_{max}^{surf}	2.5516	2.618	2.6477	2.6254	2.64	2.6104	2.6066	2.5761	2.6119	2.6064	1.5329
$\langle W \rangle$	2.4583	2.369	2.431	2.4121	2.4071	2.4189	2.4246	2.4246	2.4148	2.4282	2.5548
$\langle \Phi \rangle / Ra$	2.4333	2.4119	2.4189	2.4165	2.392	2.4182	2.4246	2.4148	2.4276	2.4281	2.31916
δ	1.02%	1.78%	0.50%	0.18%	0.63%	0.03%	< 0.01%	< 0.01%	0.16%	< 0.01%	9.22%
Case 2											
$\langle T \rangle$	0.6058	0.6034	0.6034	0.6071	0.6068	0.6029	0.603203	0.6027	0.6036	0.6049	0.5951
Nu_{top}	8.5278	8.556	8.5428	8.5217	8.6489	8.5491	8.74753	8.5693	8.5115	8.5758	9.2396
Nu_{bot}	8.3990	8.5565	8.5427	8.5217	8.6489	8.5491	8.64402	8.5407	8.4465	8.5502	9.2409
u_{RMS}	142.2020	140.6809	140.4654	141.1409	143.8518	140.3390	140.522	140.1871	140.7087	141.5940	160.499
u_{RMS}^{surf}	105.1767	104.729	104.5639	102.8500	105.0283	104.5820	104.585	104.4883	104.1228	104.9587	123.8687
u_{max}^{surf}	122.3238	121.8606	121.6508	119.4120	122.9754	121.6680	121.696	121.5673	121.766	122.1282	162.423
η_{min}	1.9853×10^{-5}	1.9900×10^{-5}	1.9853×10^{-5}	1.9850×10^{-5}	2.0800×10^{-5}	2.0173×10^{-5}	1.9607×10^{-5}	1.9854×10^{-5}	2.0600×10^{-5}	1.9853×10^{-5}	1.9880×10^{-5}
η_{max}	1.6095	1.9421	1.6317	1.7887	1.0400	1.5860	1.7959	1.8918	1.8500	1.8748	4.77×10^{-3}
$\langle W \rangle$	7.6222	7.5521	7.543	7.5199	7.64	7.5484	7.55153	7.5431	7.5665	7.5879	8.7223
$\langle \Phi \rangle / Ra$	7.6194	7.5494	7.535	7.4690	7.6422	7.5339	7.55153	7.5431	7.5585	7.5879	10.026
δ	0.04%	0.04%	0.11%	0.68%	0.03%	0.19%	<0.01%	<0.01%	0.11%	<0.01%	13.00%
Case 3											
$\langle T \rangle$	0.7286	0.7275	0.7271	0.7272	0.7241	0.7274	0.727464	0.7275	0.7275	0.7278	0.7305
Nu_{top}	3.0374	3.0298	3.0324	3.0314	3.0253	3.03025	3.0918	3.0399	3.0347	3.0371	2.9311
Nu_{bot}	2.9628	3.0298	3.0323	3.0314	3.0253	3.03025	3.03487	3.0376	2.9908	3.0410	2.9311
u_{RMS}	100.9467	100.024	99.8701	99.9917	100.197	100.018	100.127	100.0396	100.1208	100.3368	111.6121
u_{RMS}^{surf}	2.0374	2.0785	2.0916	2.0835	2.0789	2.07299	2.07301	2.0569	2.0652	2.0727	1.356
u_{max}^{surf}	2.8458	2.9029	2.9201	2.9094	2.9207	2.89495	2.89501	2.873	2.9019	2.8946	1.8806
η_{min}	4.7907×10^{-5}	4.8140×10^{-5}	4.8014×10^{-5}	4.8047×10^{-5}	4.8400×10^{-5}	4.7951×10^{-5}	4.8081×10^{-5}	4.8000×10^{-5}	4.8080×10^{-5}	4.7972×10^{-5}	10^{-4}
η_{max}	1	0.9987	0.9857	0.9988	0.9010	0.9637	0.9999	1	0.9023	1	1
$\langle W \rangle$	2.0400	2.0028	2.0340	2.0269	2.0235	2.03002	2.03482	2.0298	2.0384	2.0362	2.056
$\langle \Phi \rangle / Ra$	2.0335	2.0277	2.0304	2.0286	2.0164	2.0302	2.03482	2.0298	2.037	2.0362	1.865
δ	0.32%	1.23%	0.18%	0.08%	0.35%	0.01%	<0.01%	<0.01%	0.07%	<0.01%	9.29%
Case 4											
$\langle T \rangle$	0.5289	0.5276	0.5276	0.5289	0.5283	0.527304	0.527521	0.5274	0.5277	0.5278	0.5364
Nu_{top}	6.5572	6.6156	6.6074	6.5913	6.6356	6.61082	6.68224	6.6401	6.5912	6.6249	7.4376
Nu_{bot}	6.5243	6.6158	6.6073	6.5913	6.6356	6.61082	6.66899	6.6326	6.5834	6.6267	7.4376
u_{RMS}	79.6202	79.1358	79.0181	78.6652	79.4334	78.9903	79.0684	79.0318	79.1105	79.1996	98.8912
u_{RMS}^{surf}	75.4814	75.1727	75.0434	74.1719	74.8587	75.0606	75.0975	75.0827	74.7596	75.1903	93.5057
u_{max}^{surf}	89.2940	88.9715	88.8130	87.6118	89.1444	88.823	88.8753	88.85	88.9146	88.9848	123.046
η_{min}	1.9174×10^{-4}	1.9220×10^{-4}	1.9448×10^{-4}	1.9204×10^{-4}	1.9900×10^{-4}	1.9574×10^{-4}	1.9167×10^{-4}	1.9200×10^{-4}	1.9860×10^{-4}	1.9178×10^{-4}	1.93×10^{-4}
η_{max}	1.6773	1.9834	1.6508	1.9670	1.1800	1.6665	1.7446	1.8891	1.5200	1.8831	5.67×10^{-3}
$\langle W \rangle$	5.6512	5.6251	5.6076	5.5903	5.629	5.61012	5.61425	5.6136	5.6216	5.6235	6.751
$\langle \Phi \rangle / Ra$	5.6463	5.6174	5.6024	5.5434	5.6325	5.60152	5.61425	5.6136	5.6182	5.6235	7.786
δ	0.09%	0.14%	0.09%	0.84%	0.06%	0.15%	<0.01%	<0.01%	0.06%	<0.01%	13.29%
Case 5a											
P	0.0792	0.0763	0.07728	0.0765	0.07638	0.07691	0.0771	0.07741	0.076	0.0768	
$\langle T \rangle_{min}$	0.6543	0.6494	0.6510	0.6518	0.6491	0.651048	0.6510	0.6509	0.6514	0.6516	0.7119
$\langle T \rangle_{max}$	0.6722	0.6693	0.6689	0.6695	0.6671	0.669124	0.6690	0.669	0.6693	0.6696	0.7119
Nu_{min}^{top}	2.6950	2.6787	2.6896	2.6910	2.6902	2.6808	2.6916	2.6925	2.6808	2.6836	2.9597
Nu_{max}^{top}	7.2792	7.4019	7.3553	7.2970	7.4314	7.41844	7.4246	7.4307	7.3506	7.4041	2.9597
u_{RMS}^{min}	41.9813	41.3296	41.4920	41.7587	41.6742	41.2701	41.5434	41.2488	41.2578	41.4086	76.5018
u_{RMS}^{max}	98.8230	99.2247	98.4977	98.0040	100.538	99.9273	98.7948	98.5309	100.089	100.3461	76.5018
$\langle \Phi \rangle_{min}$	1.3447	1.3392	1.3578	1.3450	1.3351	1.3339	1.3629	1.3479	1.3307	1.3324	1.8644
$\langle \Phi \rangle_{max}$	9.2748	9.41	9.3090	9.1400	9.54	9.4818	9.3251	9.3495	9.5193	9.5289	1.8644

[a]Maximum and minimum viscosity for Case 1 (respectively, 1 and 10^{-5}) are completely determined by the boundary conditions and do not appear in the table. For each code, we also report the adopted resolution in the horizontal and vertical directions. The suffix *r* indicates whether mesh refinement near the boundaries was employed. YACC, Plaatjes, CHIC, GAIA, StreamV, and StagYY are finite volume codes; FEniCS, Fluidity, ELEFANT, and ASPECT are finite element codes; MC3D is a spectral code.
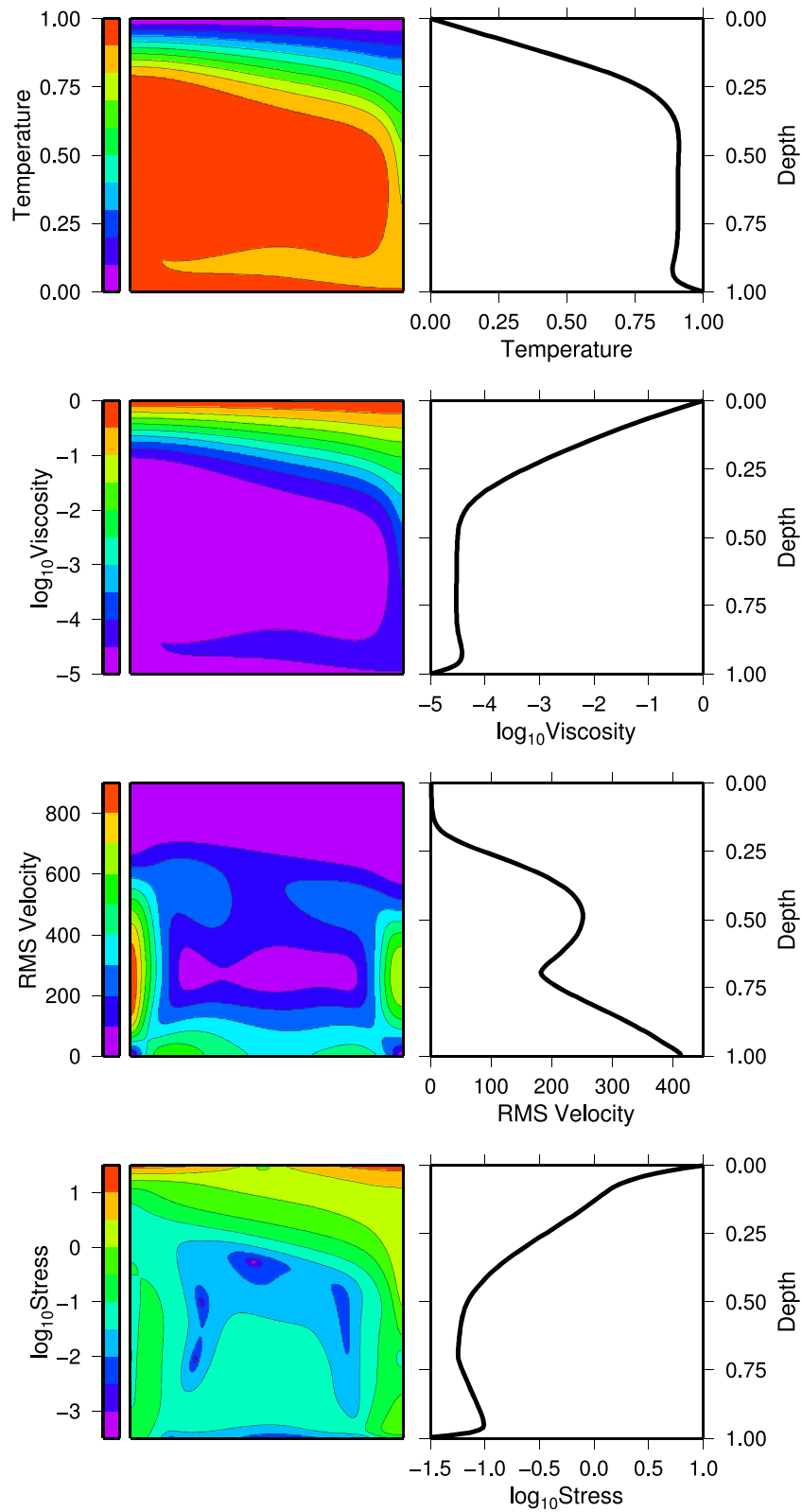
Figure 1. (left column) Steady state snapshots of temperature, viscosity, RMS velocity, second invariant of the stress tensor, and (right column) corresponding laterally averaged profiles for Case 1 obtained with the code YACC. The four profiles can be found in the Data Set S1 of the supporting information.
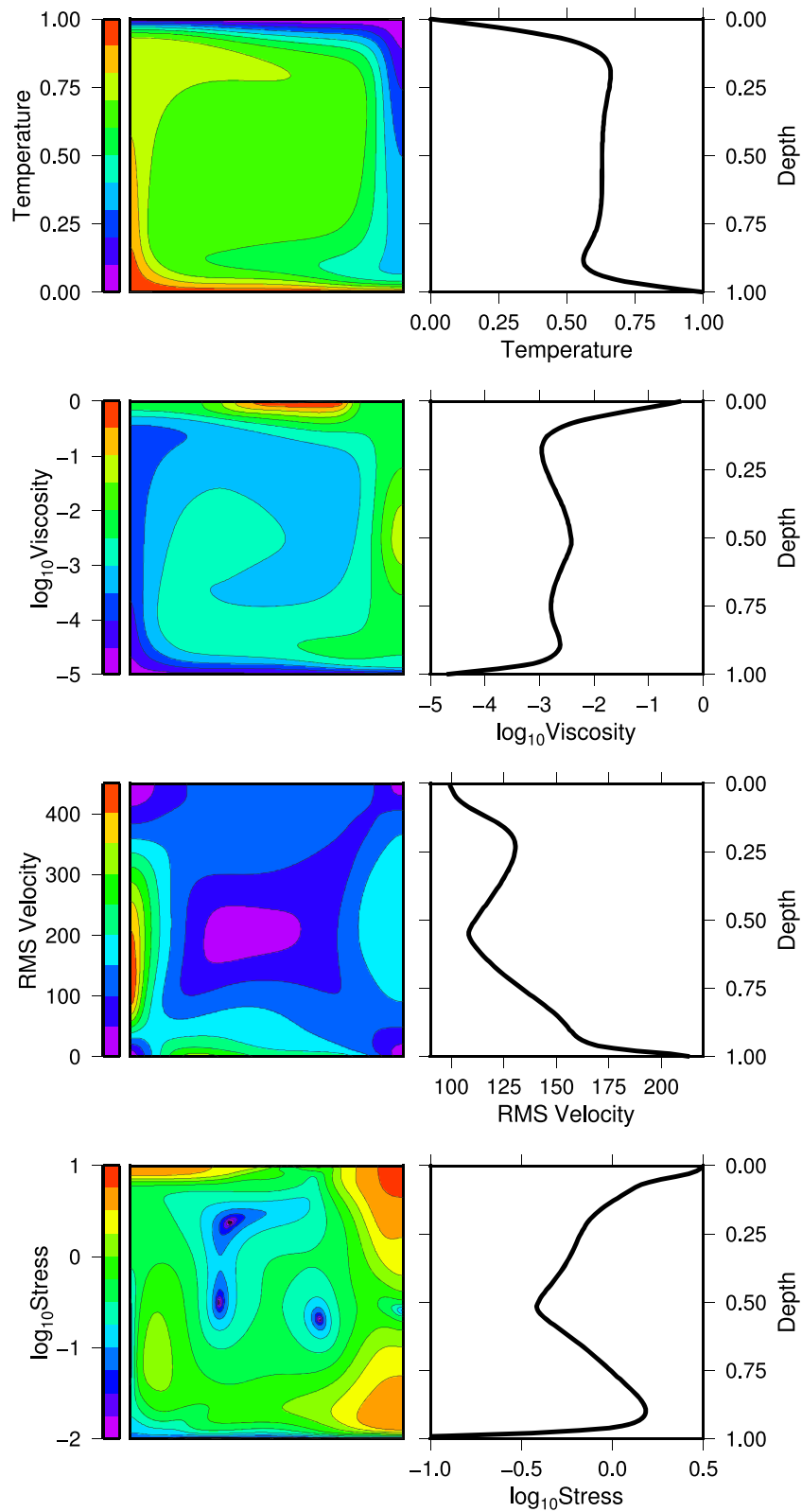
Figure 2. As in Figure 1, but for Case 2. The four profiles can be found in the Data Set S2 of the supporting information.
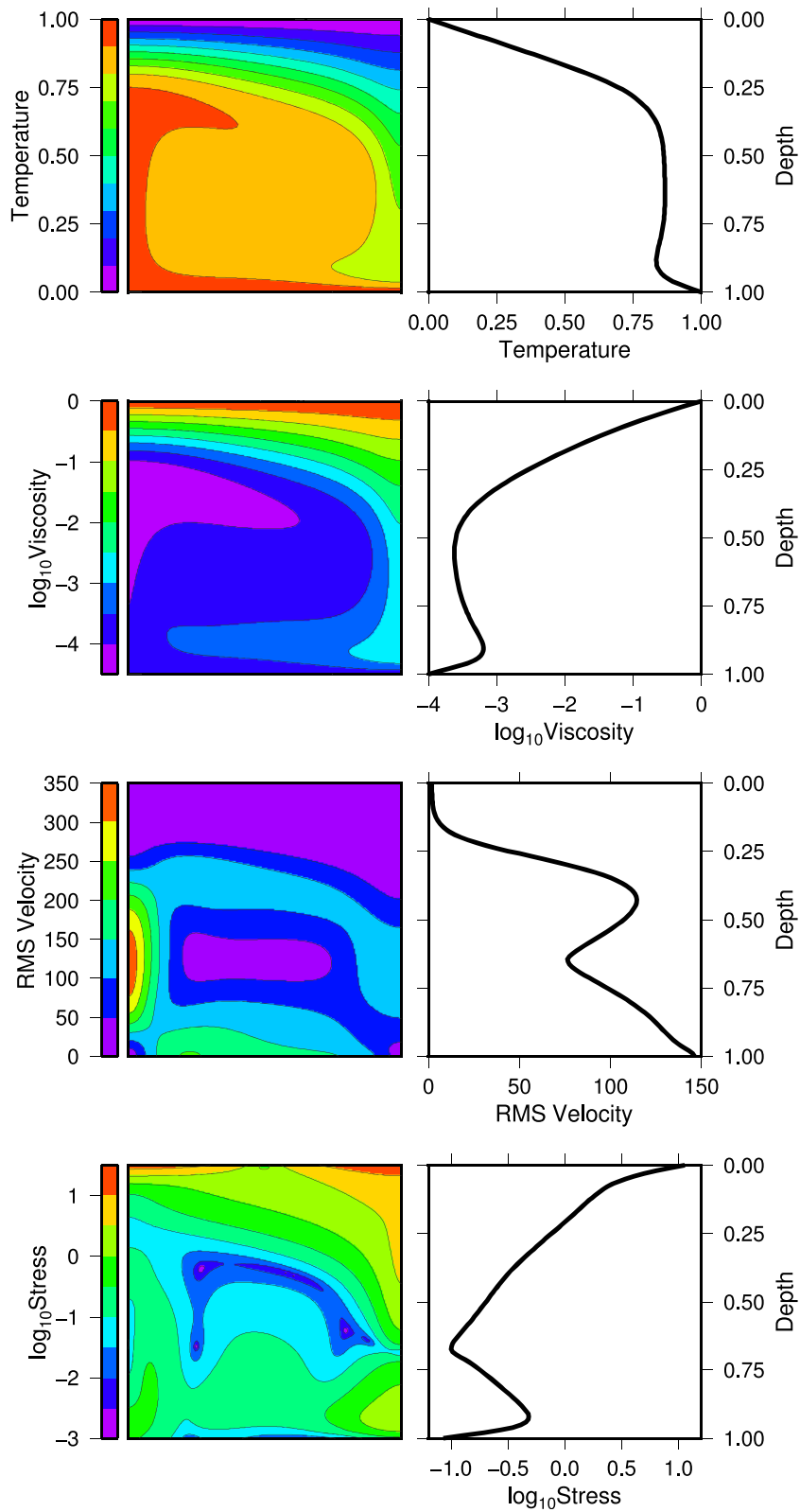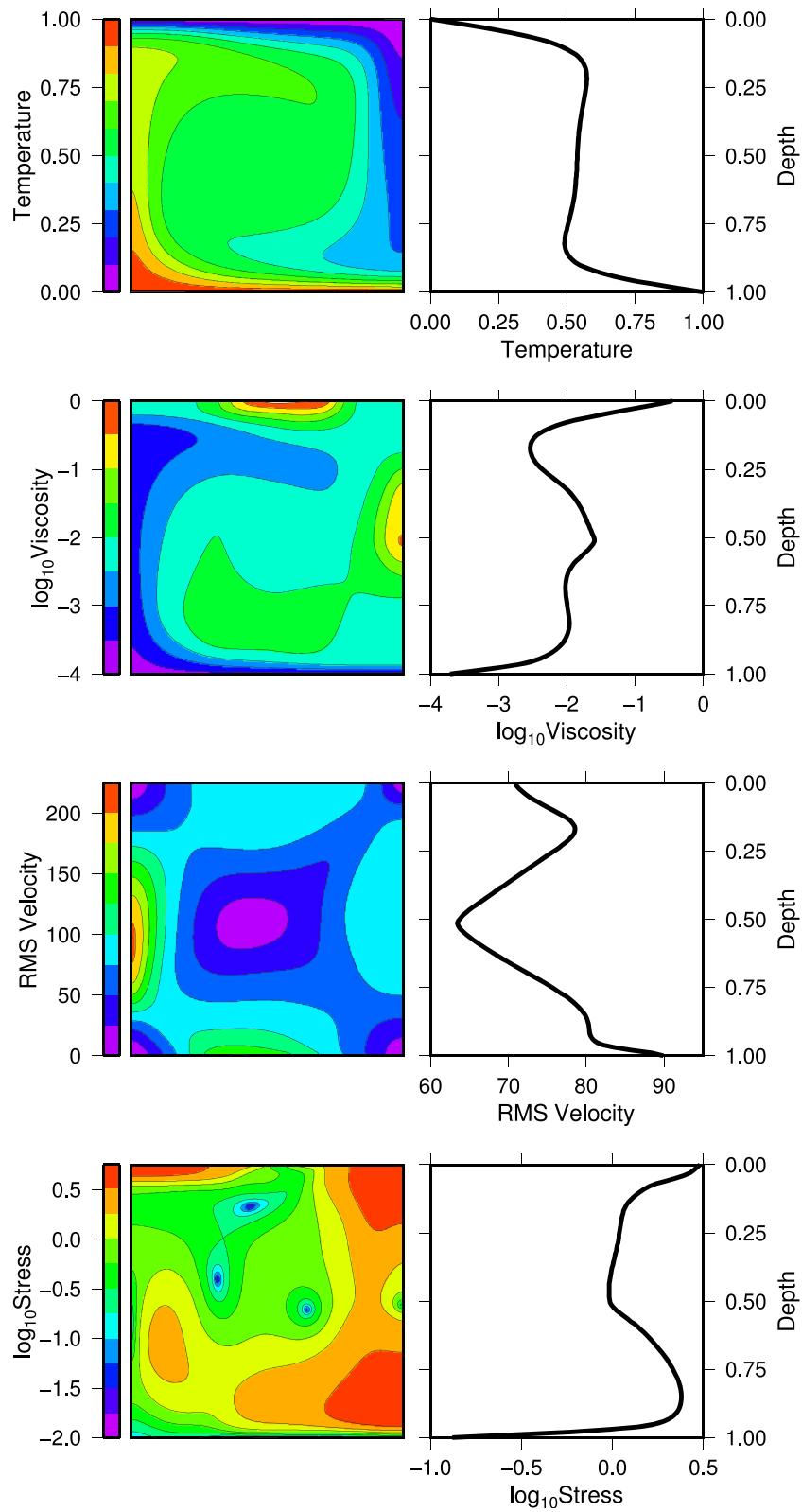
Figure 3. As in Figure 1, but for Case 3. The four profiles can be found in the Data Set S3 of the supporting information.

Figure 4. As in Figure 1, but for Case 4. The four profiles can be found in the Data Set S4 of the supporting information.

upwelling reaches the surface and the downwelling begins to sink, stresses are highest. These cause the viscosity to drop by about 2 orders of magnitude with respect to the central region beneath the surface, which is ultimately mobilized while retaining a high viscosity.

For these tests, participants were not requested to use a specific domain resolution and chose meshes between 64 × 64 elements (ASPECT) and 128 × 128 elements or cells (Fluidity and Plaatjes), either uniformly spaced or with refinement in the top and bottom boundary layers (see Table 2 for details). With these meshes, all codes produce solutions that typically differ by ~1% at most from the solutions obtained with the best refined meshes used for the resolution tests presented in section 5.2. As shown in Table 2, the codes agree very well on all diagnostic quantities. In particular, differences in the average temperature are systematically below 1%, while other quantities such as the Nusselt numbers are obviously more sensitive to the employed resolution and exhibit larger differences, although always below 5%. Upon averaging the difference between the maximum and minimum of all diagnostics (apart from the minimum and maximum viscosity) from all codes but MC3D (see below), the largest and smallest mean discrepancies are 2.5% obtained for Case 1, and 1.1%, obtained for Case 4. This is not surprising since Cases 1 and 4 are, respectively, associated with the largest and smallest effective Rayleigh numbers and thus with the largest and smallest mean temperatures and convective velocities. Clearly, the higher the Rayleigh number, the higher is the discrepancy that has to be expected if the mesh resolution is not increased. Differences in the minimum and maximum viscosity may appear larger than those observed for the other quantities. It should be noted that differences in temperature and stresses tend to be amplified when computing the viscosity because of the strongly nonlinear nature of the applied rheological relations. In addition, since η_{min} and η_{max} are attained at the domain boundaries, the exact location at which the two quantities are calculated (i.e., at node or cell/element level) contributes to the observed discrepancies, which, nevertheless, significantly diminish upon increasing the mesh resolution (see section 5.2 and Tables S2–S13 of supporting information).

For systems heated solely from below like those considered here, after reaching steady state, the top and bottom Nusselt number should be equal as no internal source of energy is considered. Interestingly, all finite volume codes, with the exception of YACC, consistently satisfy this condition at the nominal resolutions considered in this first series of tests. The differences between top and bottom Nusselt numbers obtained with YACC range from ~3% for Case 1 to ~0.5% for Case 4 and are in line with those obtained with the four finite element codes, none of which predicts the two quantities to perfectly match. This discrepancy could be indicative of a slight imbalance in the energy conservation (note that for the above codes, Nu_{top} is systematically higher than Nu_{bot}). Such imbalance could be caused by nonconservativeness properties of the advection scheme as in the case of the semi-Lagrangian advection adopted in YACC. However, the difference δ between the work done against gravity and the viscous dissipation, which is an important indicator of the accuracy with which energy is conserved [e.g., *Leng and Zhong*, 2008; *King et al.*, 2010], is always very small for all codes (typically below ~1%), with finite element codes performing slightly better than those based on finite volumes. Furthermore, as shown in the resolution tests presented in section 5.2, Nu_{top} and Nu_{bot} tend to converge to the same value upon increasing the domain resolution.

Benchmark results from MC3D exhibit the largest discrepancy with respect to the other codes. This is not surprising because, as described in section 4.11, MC3D is a spectral code in which the viscosity is averaged laterally before being used to solve the conservation equations. Although the actual values of the diagnostic quantities—of the average and surface velocities in particular—differ considerably from those obtained when using the actual viscosity distribution, it is worth noting that, despite this simplified approach, the code reproduces the expected convective regime and predicts average mantle temperatures that generally differ by less than 1% from the solutions obtained with the other codes.

5.2. Cases 1 and 2: Resolution Tests

For Cases 1 and 2, all participants conducted a series of resolution tests on more and more refined grids to assess the convergence properties of the various codes using a temperature-dependent linear rheology (Case 1) and a temperature and strain rate-dependent nonlinear rheology (Case 2). For each code, all diagnostic quantities calculated on meshes of increasing size, as well as their extrapolated values are reported in Tables S2–S13 of supporting information, while in Figure 5 we show the steady state solution for the RMS velocity from all codes as a function of the number N of grid points or elements employed in one direction
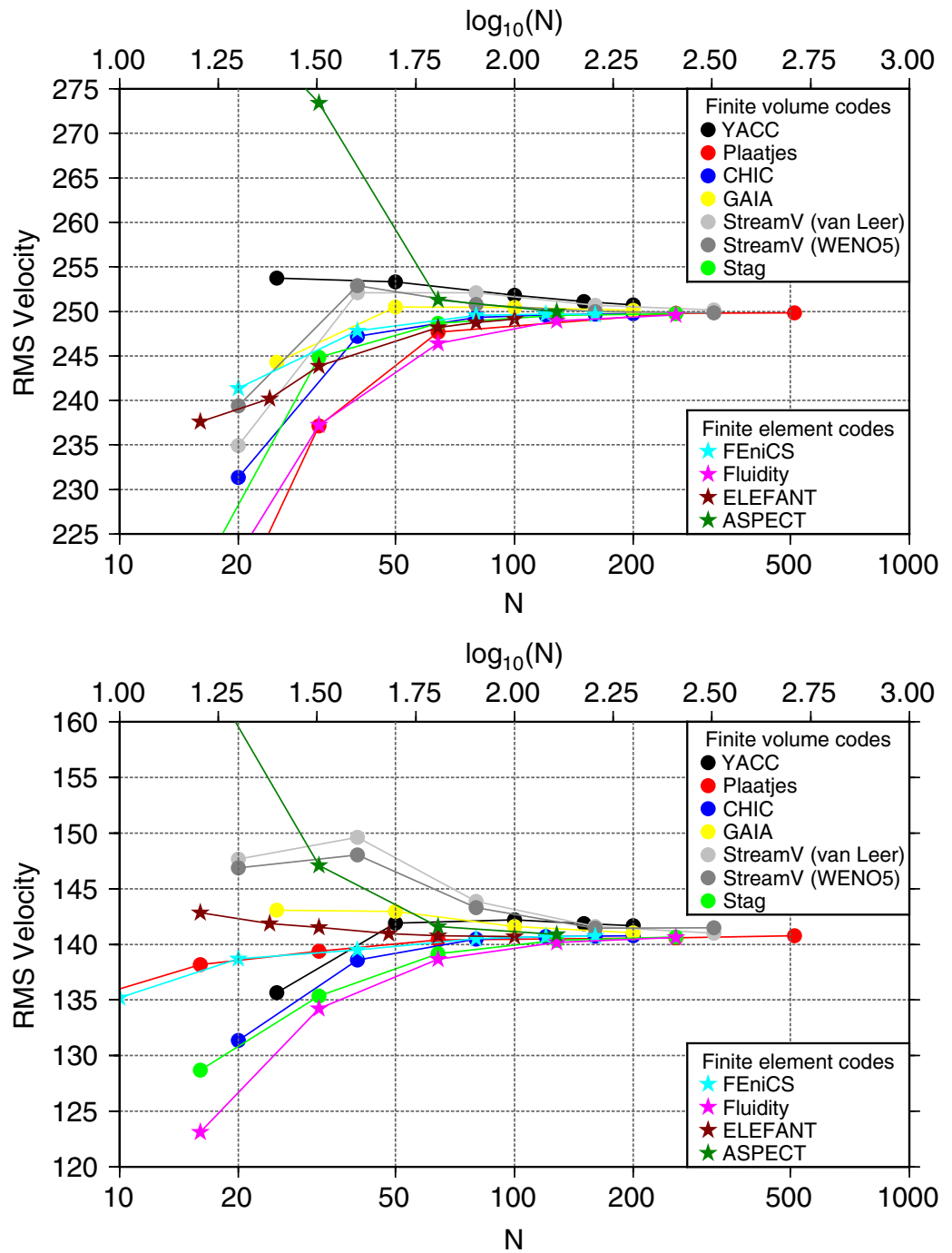
Figure 5. Steady state solution for the RMS velocity as a function of the number *N* of grid points or elements in one direction for (top) Case 1 and (bottom) Case 2. Circles refer to finite volume codes and stars to finite element codes. Numerical values used for these figures are reported in Tables S2–S13 of the supporting information.

(all codes employed the same number of grid points in both horizontal and vertical directions). In both cases, solutions lying within about 10% from those obtained on the corresponding finest meshes are achieved already for *N* = 20, with ELEFANT (brown stars) delivering on a 16 × 16 mesh an RMS velocity for Case 1 differing by less than 5% from that obtained on an 80 × 80 mesh. In general, for meshes with *N* between 50 and 100, corresponding to the grid-size typically employed when solving problems with the level of complexity of the present benchmark, the maximum spread in u_{RMS} among the various codes is quite small: around 3% for Case 1 and 4% for Case 2, indicating that the nonlinearity introduced by the
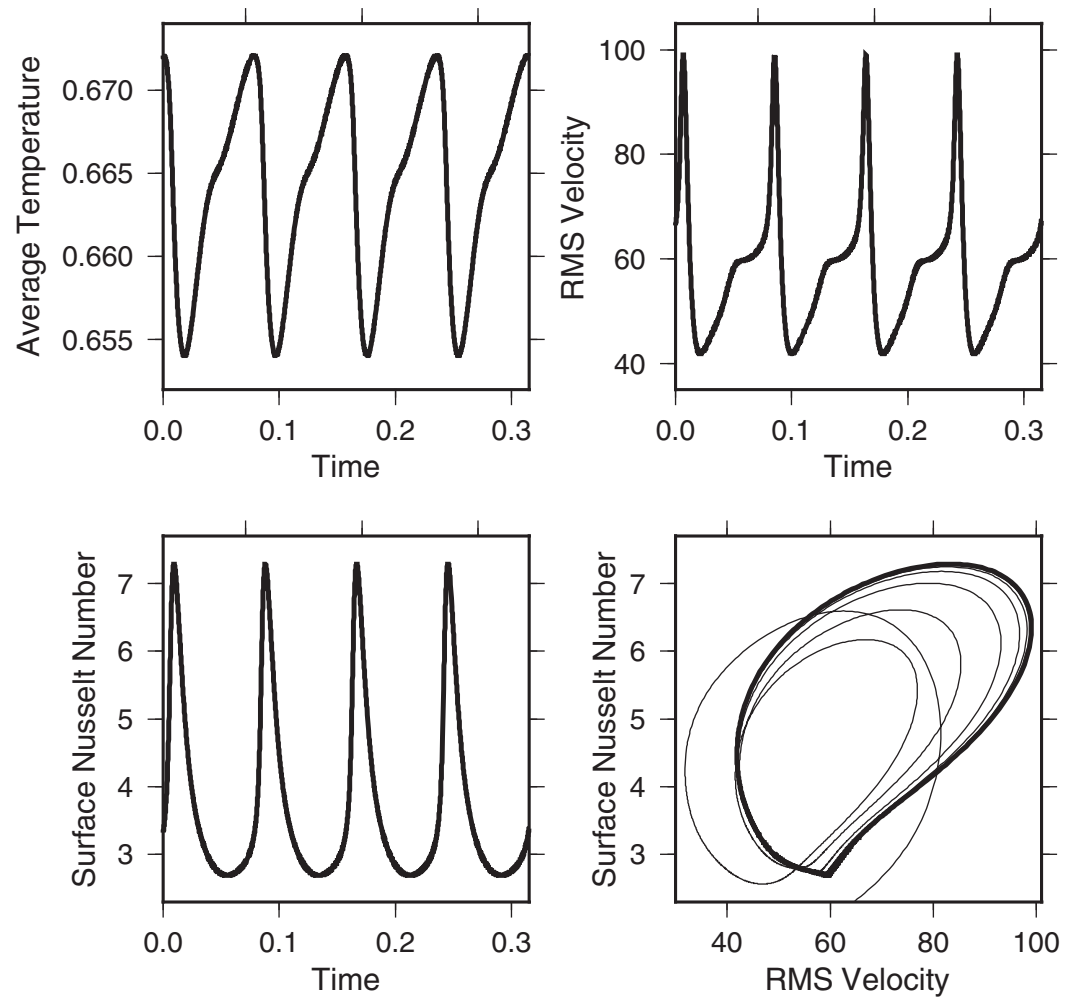
Figure 6. Time series for Case 5a calculated with YACC of the (top left) average temperature, (top right) RMS velocity, and (bottom left) surface Nusselt number over four complete cycles plotted after reaching a strictly periodic regime, and (bottom right) phase portrait of the surface Nusselt number versus RMS velocity showing how the system reaches a stable cycle. The three time series can be found in the Data Set S5 of the supporting information.

strain rate dependence of the viscosity does not impact in a significant way on the accuracy of the numerical solutions. For meshes characterized by *N* larger than 100, all codes tend to converge monotonically and deliver solutions that differ from one another by less than about 1% in both Case 1 and Case 2. When applying a Richardson extrapolation [e.g., *Roache*, 1997] to the solutions obtained on the various meshes, such differences further diminish, with coefficients of variations (i.e., standard deviation divided by mean value) of the extrapolated diagnostics comprised between 0.1% and 0.2%. Also note that for the reasons discussed in the previous section, the MC3D solution for u_{RMS} differs quite significantly from that of the other codes (see Table S12) and does not appear in Figure 5.

5.3. Case 5a: Periodic Solutions

In Case 5a, the yield stress is sufficiently large ($\sigma_Y = 4$) to cause the system to reach a stable periodic regime characterized by one single period. Figure 6 illustrates the time series of the mean temperature, RMS velocity, and surface Nusselt number over four complete cycles plotted after the system reached a strictly periodic regime; the figure also shows a phase portrait of the surface Nusselt number as a function of the RMS velocity describing the path toward the stable cycle. It is interesting to note that the maxima of the temperature are not in phase with those of the velocity (and of the Nusselt number) as one could expect because of the temperature dependence of the viscosity. Velocity maxima occur shortly after those of the temperature and correspond to a rapid overturn of the upper thermal boundary layer, which, from sluggish, becomes mobile, thereby causing the descent of a cold downwelling and, as a consequence, also an

increase of the surface Nusselt number. This behavior can be easily recognized by analyzing the data set S6 of Supporting Information, which contains a video of various 2-D fields (temperature, viscosity, RMS velocity, and stress), as well as the evolution of the surface Nusselt number as a function of time and of the RMS velocity over four complete cycles. This video also illustrates that the instability of the lithosphere is likely responsible for the observed periodic behavior, as previously reported also by *Stein and Hansen* [2008]. Stresses associated with the downwelling limb of the lithosphere, albeit comparable in magnitude with those above the plume head, are spread over a significantly larger area and ultimately cause cold parts of the upper thermal boundary layer to sink. These cool the interior causing a rapid growth of the upper lid, which remains (quasi) stagnant until the system heats up forcing again the lithosphere to become unstable, thus initiating another cycle.

As shown in Table 2, all codes but MC3D, which found a steady state solution, were able to identify this periodic regime and predicted the required diagnostic quantities with discrepancies not larger than those obtained for the steady state solutions of Cases 1–4. For example, the largest difference observed in the reported cycle periods is about 4%, while the maximum and minimum temperatures agree within less than 1%.

5.4. Case 5b: Bifurcation Analysis

Case 5b is an extension of Case 5a. Here we varied the yield stress from $\sigma_Y = 3$ to 5 with the goal of identifying the critical values at which the system transitions from a steady, mobile lid regime (for low values of σ_Y), to a periodic regime first (for intermediate values of σ_Y), and to a steady, stagnant lid regime afterward (for high values of σ_Y). The results of this analysis are shown in Figure 7 for the six finite volume codes and in Figure 8 for three finite element codes and for the spectral code MC3D. In order to assess the impact of the mesh resolution on the estimate of these critical values, each participant performed the analysis using three to five meshes of increasing resolution. At the highest resolutions tested (between 100×100 and 160×160 cells used by GAIA and StreamV, respectively) and, again, with the exception of MC3D, all codes predicted the first transition from mobile lid to periodic regime to occur for $3.7 < \sigma_Y < 3.9$. The second transition from periodic to stagnant lid regime was predicted by all codes to take place within the narrower range $4.5 < \sigma_Y < 4.6$. As already mentioned in the context of Case 5a, MC3D generally failed to predict the correct convective regime for a given value of the yield stress (Figure 8). In particular, at its highest resolution, the spectral code delivered periodic solutions for $2.8 < \sigma_Y < 3.3$. Over this interval, all other codes reported instead steady state, mobile lid solutions, thus suggesting that spatially localized variations of the viscosity are crucial when it comes to reproduce the correct regime, which cannot be captured by laterally averaging temperature and strain rate to obtain a depth-dependent viscosity. The numerical values on which Figures 7 and 8 are based are reported in Tables S14–S23 of the supporting information.

The solutions obtained from codes based on the finite volume method (Figure 7) tend to be more sensitive to the mesh resolution than those from finite element codes. For example, while the finite element codes FEniCS, Fluidity, and ASPECT predicted the second transition to occur for $4.5 < \sigma_Y < 4.6$ at all resolutions tested (from 20×20 elements used by FEniCS to 128×128 elements used by Fluidity and ASPECT), values of σ_Y between 4.3 and 4.4 have been obtained with finite volume codes at low resolutions (see, e.g., YACC and GAIA in Figure 7). A similar effect is observed for the prediction of the yield stress that characterizes the first transition.

As indicated in section 3, the initial temperature was chosen in all benchmark cases according to equation (11). Indeed it should be noted that, for Case 5b in particular, the occurrence of a steady state or periodic regime for a given value of the yield stress can be sensitive to the choice of the initial conditions. To illustrate this, we show in Figure 9 the time evolution of the RMS velocity calculated with YACC assuming $\sigma_Y = 3.4$ and using different initial temperatures T_0 from 0.1 to 0.9 instead of the linear profile of equation (11) (the initial profile assumed here consists of an isothermal mantle with temperature T_0, two thermal boundary layers with a nondimensional thickness of 0.1 and a sinusoidal perturbation with an amplitude of 0.01 to initiate convection). While for $T_0 \leq 0.6$, the system evolves to a steady state, mobile lid regime, which is also what all codes predicted using equation (11) as initial condition, for $T_0 \geq 0.7$ a stable periodic regime is obtained. The inset of Figure 9 illustrates the initial part of the evolution with the black dashed line marking the minimum u_{RMS}^{min} of the velocity obtained from the periodic solutions. If the initial temperature is high ($T_0 \geq 0.7$ in this case), the viscosity is sufficiently low to guarantee that the initial velocity is close enough to or larger than u_{RMS}^{min}, which ensures that the system eventually exhibits a periodic behavior. Note that u_{RMS}^{min} is
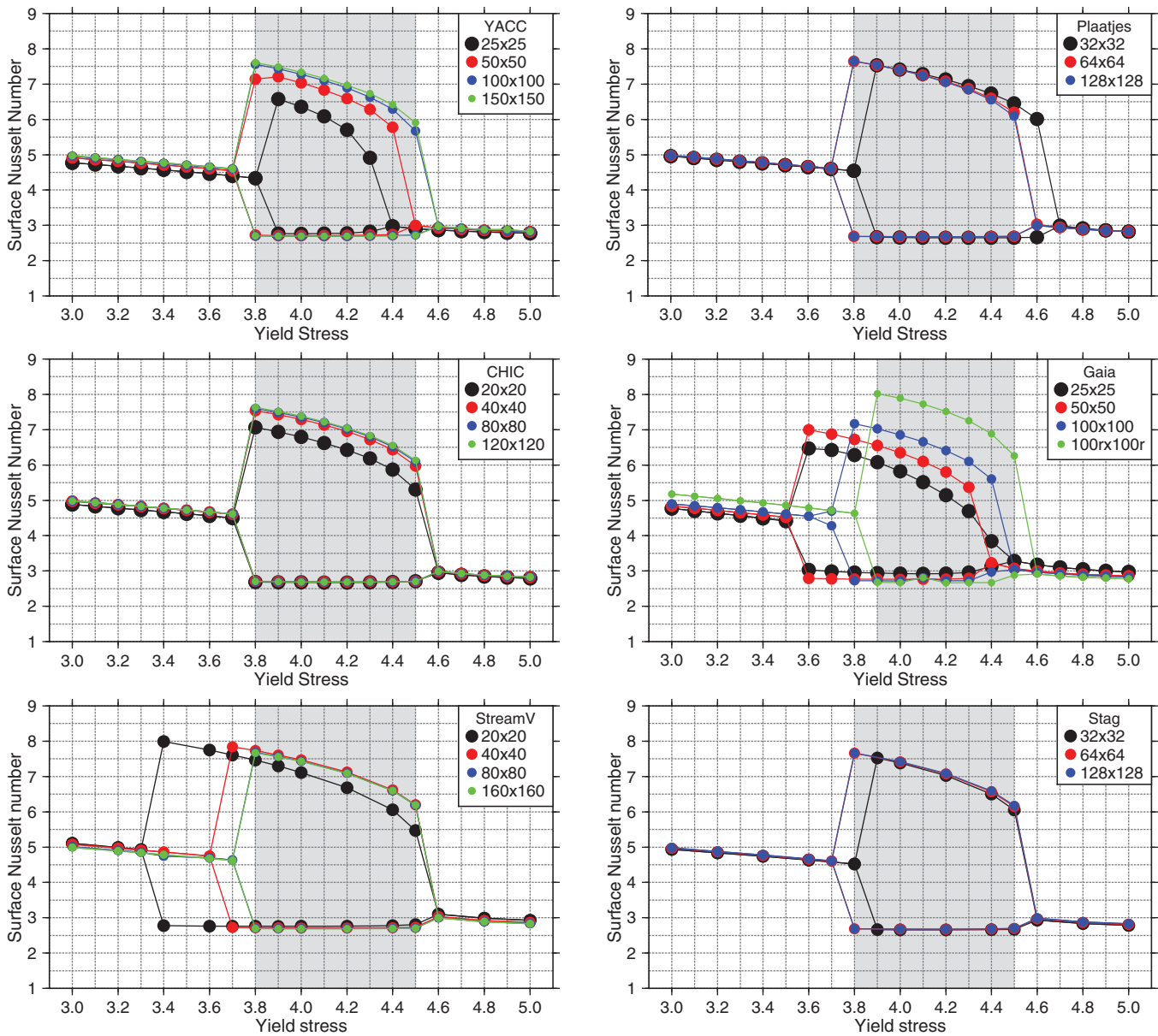
Figure 7. Bifurcation diagram showing the maximum and minimum surface Nusselt number as a function of the yield stress for the six finite volume codes ran on more and more refined meshes. Note that in the mobile and stagnant lid regimes, the two quantities coincide. The gray area indicates the range of yield stresses for which a given code ran at its highest resolution obtained a periodic regime. Numerical values used for this figure are reported in Tables S14–S19 of the supporting information.

exceeded also for $T_0 \leq 0.6$ but only at later times. What actually determines whether the system evolves into a periodic or steady (mobile lid) regime is then its initial temperature and, in turn, its initial viscosity distribution whose effects are reflected in the time evolution of the velocity. The transition from periodic to stagnant lid regime seems instead to be better defined and for $\sigma_Y > 4.5$ we did not identify a sensitive dependence on initial conditions.

6. Conclusions

We presented the first suite of tests to benchmark numerical simulations of thermal convection of a viscoplastic fluid with temperature, pressure, and strain rate-dependent viscosity in a two-dimensional square cavity. Five simple tests were designed to obtain steady state convection (with a mobile or stagnant lid) or
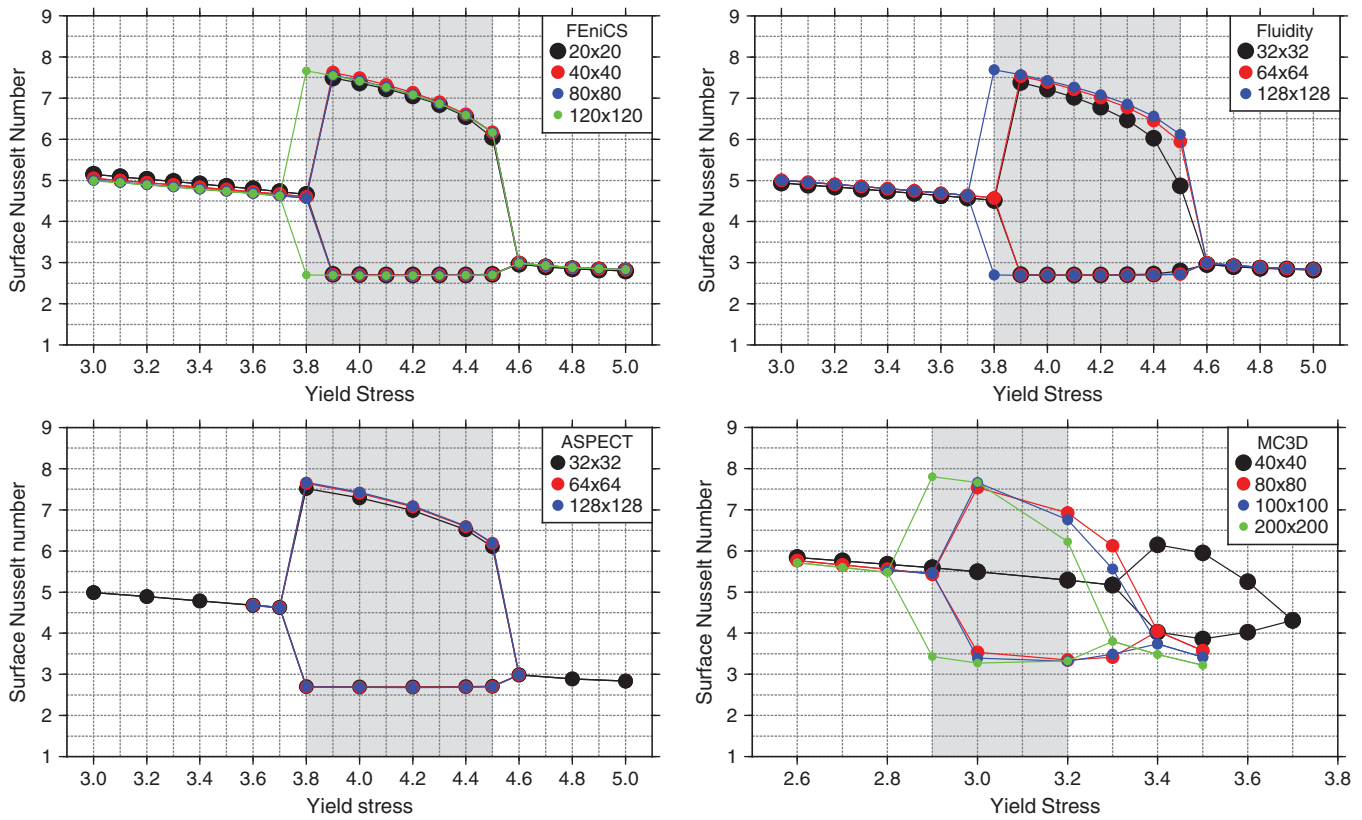
Figure 8. As in Figure 7 but for three finite element codes and the spectral code MC3D. Numerical values used for this figure are reported in Tables S20–S23 of the supporting information.

periodic convection as a function of the yield stress. In all tests and for all requested diagnostic quantities, we found a good agreement among six finite volume codes and four finite element codes, both in the presence of linear and nonlinear rheologies. For two of the five reference benchmark cases (Cases 1 and 2), all
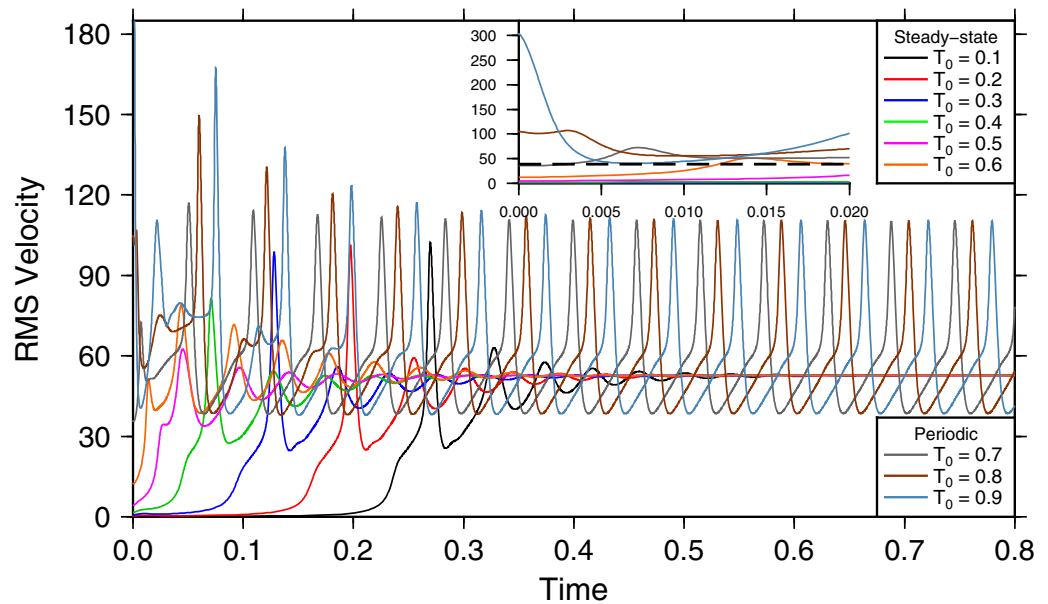
Figure 9. Time evolution of the RMS velocity calculated with YACC for Case 5b with $\sigma_Y = 3.4$ and different initial temperatures T_0, from 0.1 to 0.9. The inset shows the evolution of u_{RMS} up to a nondimensional time of 0.02, with the black dashed line denoting the minimum of u_{RMS} of the periodic solutions.

participants carried out a series of convergence tests using meshes with resolutions form very coarse to highly refined (e.g., Plaatjes was tested on meshes from 8×8 cells to 512×512 cells). We found that the nonlinearity introduced by the dependence of the viscosity on the strain rate does not significantly impact on the accuracy of the numerical solutions, which, on meshes of $\sim 100 \times 100$ cells/elements, typically differ by less than 1% from those obtained with the same code on grids with $\sim 200 \times 200$ cells/elements or more. In addition, we performed a bifurcation analysis (Case 5b) aimed at identifying the critical values of the yield stress for which the convective regime changes from mobile lid to periodic and from periodic to stagnant lid. Also in this case, we found a good agreement among the different codes with finite volume codes generally exhibiting a more pronounced sensitivity to the mesh resolution with respect to finite element codes. A spectral code (MC3D) capable to treat only a depth-dependent viscosity obtained from laterally averaging temperature and strain rate was also used to carry out all tests. Although, with this approach, reasonably accurate solutions could be achieved in the steady state cases (for the average temperature and Nusselt numbers in particular), the critical yield stresses at which the transition to different regimes was observed were remarkably different from those obtained with the other codes.

The majority of the codes involved in this benchmark effort can also work with more complex geometries using the same solution framework adopted here. Additional benchmarks will certainly be needed to reliably assess the accuracy of numerical implementations in geometries other than a simple 2-D box. Nevertheless, we expect that our tests will be a useful tool to at least partially validate new implementations of viscoplastic thermal convection in cylindrical and spherical domains that are more appropriate for modeling mantle dynamics.

References

Amestoy, P., I. Duff, J.-Y. L'Excellent, and J. Koster (2001), A fully asynchronous multifrontal solver using distributed dynamic scheduling, *SIAM J. Matrix Anal. Appl.*, *23*(1), 15–41.

Amestoy, P., A. Guermouche, J.-Y. L'Excellent, and S. Pralet (2006), Hybrid scheduling for the parallel solution of linear systems, *Parallel Comput.*, *32*(2), 136–156.

Balay, S., W. D. Gropp, L. C. McInnes, and B. F. Smith (1997), Efficient management of parallelism in object-oriented numerical software libraries, in *Modern Software Tools for Scientific Computing*, pp. 163–202, Birkhauser Boston Inc., Boston, Mass.

Bangerth, W., R. Hartmann, and G. Kanschat (2007), deal.II—A general purpose object oriented finite element library, *ACM Trans. Math. Software*, *33*(4), 24/1–24/27.

Blankenbach, B., et al. (1989), A benchmark comparison for mantle convection codes, *Geophys. J. Int.*, *98*, 23–38.

Buiter, S., A. Y. Babeyko, S. Ellis, T. V. Gerya, B. J. P. Kaus, A. Kellner, G. Schreurs, and Y. Yamada (2006), The numerical sandbox: Comparison of model results for a shortening and an extension experiment, *Geol. Soc. Spec. Publ.*, *253*(1), 29–64.

Burstedde, C., L. C. Wilcox, and O. Ghattas (2011), p4est: Scalable algorithms for parallel adaptive mesh refinement on forests of octrees, *SIAM J. Sci. Comput.*, *33*(3), 1103–1133, doi:10.1137/100791634.

Busse, F., et al. (1994), 3D convection at infinite Prandtl number in Cartesian geometry—A benchmark comparison, *Geophys. Astrophys. Fluid Dyn.*, *75*(1), 39–59.

Crameri, F., H. Schmeling, G. J. Golabek, T. Duretz, R. Orendt, S. J. H. Buiter, D. A. M. B. J. P. Kaus, T. V. Gerya, and P. J. Tackley (2012), A comparison of numerical surface topography calculations in geodynamic modelling: An evaluation of the "sticky air" method, *Geophys. J. Int.*, *189*(1), 38–54.

Davies, D. R., C. R. Wilson, and S. C. Kramer (2011), Fluidity: A fully unstructured anisotropic adaptive mesh computational modeling framework for geodynamics, *Geochem. Geophys. Geosyst.*, *12*, Q06001, doi:10.1029/2011GC003551.

Foley, B., and T. Becker (2009), Generation of plate-like behavior and mantle heterogeneity from a spherical, viscoplastic convection model, *Geochem. Geophys. Geosyst.*, *10*, Q08001, doi:10.1029/2009GC002378.

Frank-Kamenetskii, D. (1969), *Diffusion and Heat Transfer in Chemical Kinetics*, Plenum, N. Y.

Gable, C. W., R. J. O'Connell, and B. J. Travis (1991), Convection in three dimensions with surface plates: Generation of toroidal flow, *J. Geophys. Res.*, *96*, 8391–8405, doi:10.1016/j.pepi.2008.07.036.

Gerya, T., and D. Yuen (2003), Characteristic-based marker-in-cell method with conservative finite-differences schemes for modelling geological flows with strongly variable transport properties, *Phys. Earth Planet. Inter.*, *140*, 293–318.

Harder, H., and U. Hansen (2005), A finite-volume solution method for thermal convection and dynamo problems in spherical shells, *Geophys. J. Int.*, *161*, 522–532.

Harten, A. (1983), High resolution schemes for hyperbolic conservation laws, *J. Comput. Phys.*, *49*, 357–393.

Hernlund, J. W., and P. J. Tackley (2008), Modeling mantle convection in the spherical annulus, *Phys. Earth Planet. Inter.*, *171*(1–4), 48–54.

Heroux, M. A., et al. (2005), An overview of the Trilinos project, *ACM Trans. Math. Software*, *31*(3), 397–423.

Hughes, T. J. R., and A. Brooks (1982), Streamline upwind Petrov-Galerkin formulations for convection dominated flows with particular emphasis on the incompressible Navier-Stokes equations, *Comput. Methods Appl. Mech. Eng.*, *32*, 199–259.

Hüttig, C., and K. Stemmer (2008a), The spiral grid: A new approach to discretize the sphere and its application to mantle convection, *Geochem. Geophys. Geosyst.*, *9*, Q02018, doi:10.1029/2007GC001581.

Hüttig, C., and K. Stemmer (2008b), Finite volume discretization for dynamic viscosities on Voronoi grids, *Phys. Earth Planet. Inter.*, *171*, 137–146.

Hüttig, C., N. Tosi, and W. Moore (2013), An improved formulation of the incompressible Navier-Stokes equations with variable viscosity, *Phys. Earth Planet. Inter.*, *220*, 11–18, doi:10.1016/j.pepi.2013.04.002.

Jiang, G. S., and C. W. Shu (1996), Efficient implementation of Weighted ENO schemes, *J. Comput. Phys.*, *126*, 202–228.

King, S., C. Lee, P. van Keken, W. Leng, S. Zhong, E. Tan, N. Tosi, and M. Kameyama (2010), A community benchmark for 2D Cartesian compressible convection in the Earth's mantle, *Geophys. J. Int.*, *180*, 73–87, doi:10.1111/j.1365-246X.2009.04413.x.

Kramer, S. C., C. R. Wilson, and D. R. Davies (2012), An implicit free-surface algorithm for geodynamical simulations, *Phys. Earth Planet. Inter.*, *194*, 25–37, doi:10.1016/j.pepi.2012.01.001.

Kronbichler, M., T. Heister, and W. Bangerth (2012), High accuracy mantle convection simulation through modern numerical methods, *Geophys. J. Int.*, *191*(1), 12–29, doi:10.1111/j.1365-246X.2012.05609.x.

Le Voci, G., D. R. Davies, S. Goes, S. C. Kramer, and C. R. Wilson (2014), A systematic 2-D investigation into the mantle wedge's transient flow regime and thermal structure: Complexities arising from a hydrated rheology and thermal buoyancy, *Geochem. Geophys. Geosyst.*, *15*, 28–51, doi:10.1002/2013GC005022.

Leng, W., and S. Zhong (2008), Viscous heating, adiabatic heating and energetic consistency in compressible mantle convection, *Geophys. J. Int.*, *173*, 693–702, doi:10.1111/j.1365-246X.2008.03745.x.

Leng, W., and S. Zhong (2011), Implementation and application of adaptive mesh refinement for thermochemical mantle convection studies, *Geochem. Geophys. Geosyst.*, *12*, Q04006, doi:10.1029/2010GC003425.

Logg, A., K.-A. Mardal, and G. N. Wells (2012), Automated Solution of Differential Equations by the Finite Element Method, *Lecture Notes in Computational Science and Engineering*, vol. 84, Springer, Berlin Heidelberg, doi:10.1007/978-3-642-23099-8.

May, D., and L. Moresi (2008), Preconditioned iterative methods for Stokes flow problems arising in computational geodynamics, *Phys. Earth Planet. Int.*, *171*, 33–47, doi:10.1016/j.pepi.2008.07.036.

Noack, L., A. Rivoldini, and T. Van Hoolst (2015), CHIC—Coupling habitability, interior and crust: A new code for modeling the thermal evolution of planets and moons, INFOCOMP 2015, pp. 84–90, IARIA. [Available at http://www.thinkmind.org/index.php?view=article&article id=infocomp_2015_4_20_60030.]

Patankar, S. (1980), Hemisphere series on computational methods in mechanics and thermal science, in *Numerical Heat Transfer and Fluid Flow*, Taylor and Francis, Washington, D. C.

Roache, P. J. (1997), Quantification of uncertainty in computational fluid dynamics, *Annu. Rev. Fluid Mech.*, *29*(1), 123–160.

Roe, P. L. (1986), Characteristic-based schemes for the Euler equations, *Annu. Rev. Fluid Mech.*, *18*(1), 337–365.

Samuel, H. (2012), Time-domain parallelization for computational geodynamics, *Geochem. Geophys. Geosyst.*, *13*, Q01003, doi:10.1029/2011GC003905.

Samuel, H. (2014), A level set two-way wave equation approach for Eulerian interface tracking, *J. Comput. Phys.*, *259*, 617–635.

Samuel, H., and M. Evonuk (2010), Modeling advection in geophysical flows with particle level sets, *Geochem. Geophys. Geosyst.*, *11*, Q08020, doi:10.1029/2010GC003081.

Schenk, O., and K. Gärtner (2000), Solving unsymmetric sparse systems of linear equations with PARDISO, *Future Gener. Comput. Syst.*, *20*(3), 475–487.

Schenk, O., and K. Gärtner (2006), On fast factorization pivoting methods for symmetric indefinite systems, *Electron. Trans. Numer. Anal.*, *23*, 158–179.

Schmeling, H., et al. (2008), A benchmark comparison of spontaneous subduction models—Towards a free surface, *Phys. Earth Planet. Inter.*, *171*(1), 198–223.

Sleijpen, G. L. G., and D. R. Fokkema (1993), BiCGstab(ℓ) for linear equations involving unsymmetric matrices with complex spectrum, *Electron. Trans. Numer. Anal.*, *1*, 11–32.

Smolarkiewicz, P. K. (1984), A fully multidimensional positive definite advection transport algorithm with small implicit diffusion, *J. Comput. Phys.*, *54*, 325–362.

Spiegelman, M., and R. Katz (2006), A semi-Lagrangian Crank-Nicolson algorithm for the numerical solution of advection-diffusion problems, *Geochem. Geophys. Geosyst.*, *7*, Q04014, doi:10.1029/2005GC001073.

Stein, C., and U. Hansen (2008), Plate motions and the viscosity structure of the mantle insights from numerical modelling, *Earth Planet. Sci. Lett.*, *272*(1), 29–40.

Stein, C., and U. Hansen (2014), Numerical investigation of a layered temperature-dependent viscosity convection in comparison to convection with a full temperature dependence, *Phys. Earth Planet. Inter.*, *226*, 1–13.

Stein, C., J. Schmalzl, and U. Hansen (2004), The effect of rheological parameters on plate behaviour in a self-consistent model of mantle convection, *Phys. Earth Planet. Inter.*, *142*(3), 225–255.

Stein, C., J. Lowman, and U. Hansen (2014), A comparison of mantle convection models featuring plates, *Geochem. Geophys. Geosyst.*, *15*, 2689–2698, doi:10.1002/2013GC005211.

Tackley, P. (2000), Self-consistent generation of tectonic plates in time-dependent, three-dimensional mantle convection simulations: 1. Pseudo-plastic yielding, *Geochem. Geophys. Geosyst.*, *1*(8), 1021, doi:10.1029/2000GC000036.

Tackley, P. (2008), Modelling compressible mantle convection with large viscosity contrasts in a three-dimensional spherical shell using the Yin-Yang grid, *Phys. Earth Planet. Inter.*, *1–4*, 7–18, doi:10.1016/j.pepi.2008.08.005.

Tackley, P. J. (1993), Effects of strongly temperature-dependent viscosity on time-dependent, 3-dimensional models of mantle convection, *Geophys. Res. Lett.*, *20*, 2187–2190.

Tackley, P. J. and S. Xie (2003), Stag3D: A code for modeling thermo-chemical multiphase convection in Earth's mantle, in *Second MIT Conference on Computational Fluid and Solid Mechanics*, edited by K. J. Bathe, pp. 1524–1528, Elsevier, Oxford, U. K.

Thieulot, C. (2011), FANTOM: Two- and three-dimensional numerical modelling of creeping flows for the solution of geological problems, *Phys. Earth Planet. Inter.*, *188*, 47–68.

Thieulot, C. (2014), ELEFANT: A user-friendly multipurpose geodynamics code, *Solid Earth Discuss.*, *6*, 1949–2096.

Tosi, N., D. Yuen, and O. Čadek (2010), Dynamical consequences in the lower mantle with the post-perovskite phase change and strongly depth-dependent thermodynamic and transport properties, *Earth Planet. Sci. Lett.*, *298*, 229–243, doi:10.1016/j.epsl.2010.08.001.

Travis, B. J., C. Anderson, J. Baumgardner, C. W. Gable, B. H. Hager, R. J. O'Connell, P. Olson, A. Raefsky, and G. Schubert (1990), A benchmark comparison of numerical-methods for infinite Prandtl number thermal-convection in 2-dimensional Cartesian geometry, *Geophys. Astrophys. Fluid Dyn.*, *135*(3–4), 137–160.

Trompert, R., and U. Hansen (1996), The application of a finite volume multigrid method to three-dimensional flow problems in a highly viscous fluid with a variable viscosity, *Geophys. Astrophys. Fluid Dyn.*, *83*, 261–291.

Trompert, R., and U. Hansen (1998), Mantle convection simulations with rheologies that generate plate-like behaviour, *Nature*, *395*(6703), 686–689.

van Heck, H., and P. Tackley (2008), Planforms of self-consistently generated plates in 3D spherical geometry, *Geophys. Res. Lett.*, *35*, L19312, doi:10.1029/2008GL035190.

van Keken, P. E., S. D. King, H. Schmeling, U. R. Christensen, and D. N. M. Doin (1997), A comparison of methods for the modeling of thermochemical convection, *J. Geophys. Res.*, *102*, 22,477–22,495, doi:10.1029/97JB01353.

van Keken, P. E., et al. (2008), A community benchmark for subduction zone modeling, *Phys. Earth Planet. Inter.*, *171*(1), 187–197.

van Leer, B. (1979), Towards the ultimate conservative difference scheme, V. A second order sequel to Godunov's method, *J. Comput. Phys.*, *32*, 101–136.

Vynnytska, L., M. E. Rognes, and S. R. Clark (2013), Benchmarking FEniCS for mantle convection simulations, *Comput. Geosci.*, *50*, 95–105.

Wessel, P., W. Smith, R. Scharroo, J. Luis, and F. Wobbe (2013), Generic mapping tools: Improved version released, *Eos Trans. AGU*, *94*(45), 409–410.

Zhong, S., A. McNamara, E. Tan, L. Moresi, and M. Gurnis (2008), A benchmark study on mantle convection in a 3-D spherical shell using CitcomS, *Geochem. Geophys. Geosyst.*, *9*, Q10017, doi:10.1029/2008GC002048.